Polyscale technology for developing near infrared fluorescence bioimaging system based on novel synthese approaches for rare-earth doped nanophspors

K. Soga[1,2,3] and Y. Nagasaki[2,3,4]

Fluorescence bioimaging is one of the key technologies for biomedical science and engineering. Major issues of the current fluorescence bioimaiging are colour fading of the fluorescent probes, phototoxicity and strong light scattering due to the use of a short wavelength excitation light, an ultraviolet or visible light. The use of fluorescent probes to be excited by longer wavelength excitation light, i.e. near infrared light, should solve all of the above issues. In this paper, materials and system developments for the fluorescence bioimaging system with near infrared excitation are reviewed. The development of the system is based on 'polyscale technology,' a post-nanotechnology by cooperative works of the technologies in various scales. The concept and example of the 'polyscale technology' are also described.

Keywords: Bioimaging, Polyscale, Upconversion, Rare-earth, Near infrared, NIR

Introduction

Over the long history of materials sciences, atoms and molecules, with certain electronic, atomic and molecular structures, are academically recognised as basis of functions of materials. On the other hand, in terms of practical use of materials, the materials technologies are also developed as macroscopic technology for forming and shaping the materials to be devices or tools. Referring the scales of those technologies, the former one can be categorised as 'atomic' technology in picometres and subnanometres. The latter 'macroscopic' ones are located from metre down to millimetre scale ranges, where an optical microscope can be used. In between the scales, 'nano' scale is located. Since the word 'nanotechnology' was used by R. P. Feynman in 1959, almost 50 years has passed. The famous 'nano-technology initiative' by Bill Clinton initiated the nanotechnology boom and enormous technologies in 'nano' scale have been developed in the decades. The fruits of the nanotechnology in the decades in materials processing and characterisations are nanostructure forming technologies, nanoassembling technologies and high resolution observations of the materials in nano scale in various methods. Finally, the nanotechnology is connected with the above 'atomic' and 'macroscopic' technologies and now, it is time to go for 'polyscale technology' throughout the scales. The 'polyscale technology' is a coinage expresses post-nanotechnology. The meaning is that by connecting traditional atomic- and macroscale technologies together with recent intensively developed nanotechnologies, one can apply the academic knowledge to practical industries. A piece of crystal starts growing in atomic scale and grows to have passive and active functions in nanoscale and microscale. It eventually grows to be used in sizes in micrometre to millimetre. The beauty of Jewel is scientifically discussed in atomic and nanoscales as for the colours, refractive index, transparency and hardness, while the brilliancy and the looks are dominated in micrometre to millimetre scale in terms of the polishing and cutting. In the case of drug delivery system (DDS) technology, for designing a medicine, the authors use the atomic and molecular technologies. The drug should be assembled in a bio-functional carrier by the nanotechnologies. The delivery itself is a design in microscale to find out the best route and method to deliver the medicine to proper cells. Photonic materials, for example nanophosphors, are designed by using quantum mechanics in the atomic scale, synthesised and modified by functional polymers in the nano scale, and finally used for bioimaging in the micrometre to millimetre scale. Academic knowledge of photonic, electric, magnetic and thermoelectric properties of materials is applied to design materials in atomic and nanoscales. Physical, chemical, biological and geological knowledge of properties and processing of

[1]Department of Materials Science and Technology, Tokyo University of Science, 2641 Yamazaki, Noda, Chiba 278-8510, Japan
[2]Polyscale Technology Research Center, Tokyo University of Science, 2641 Yamazaki, Noda, Chiba 278-8510, Japan
[3]Center for Tsukuba Advanced Research Alliance, University of Tsukuba, Ten-noudai, Tsukuba, Ibaraki 305-8573, Japan
[4]Tsukuba Research Center for Interdisciplinary Materials Science, University of Tsukuba, Ten-noudai, Tsukuba, Ibaraki 305-8573, Japan

*Corresponding author, email mail@ksoga.com

Received 26 January 2009; accepted 1 May 2009
DOI 10.1179/143307510X12599329343402

materials can only be utilised by encountering all technologies from the atomic technologies to the macroscopic technologies through the nanotechnology. The 'polyscale technology' can, in other words, convert academic knowledge to 'make' materials into industrial knowledge to 'use' materials. For industrialising the academic knowledge in atomic or nanoscales, the authors always need the concept overview from the atomic scale to the macroscopic scale. We call the technology throughout the scales to be 'polyscale technology.' Now the importance of the 'polyscale technology' should be emphasised as a post-nanotechnology after the tremendous development of nanotechnologies in the decade. The 'scale' does not only mean a measuring unit but also mean the field of research. The 'polyscale technology' includes the interdisciplinary collaboration among the basic sciences such as physics, chemistry, biology, geology and basic engineering for a practical use of technologies.

Fluorescence bioimaging (FBI) is one of the key technologies for biomedical researches. In the current imaging system, UV or visible lights are used for exciting organic or quantum dot fluorescent probes. However, since the short wavelength light has high quantum energy, the phototoxicity of the excitation light on the biological substances and the probes themselves is the most serious problem in the FBI technology. The authors have been proposing new FBI systems with near infrared (NIR) excitation by using rare-earth doped ceramic nanophosphors (RED-CNP). As represented by Er doped optical amplifiers for telecommunication[1] or Nd : YAG lasers for various purposes,[2] rare-earth doped ceramic materials can emit efficient fluorescence in the NIR region. The design, fabrication of the materials and the development of the imaging system of the NIR-FBI system require technologies in various scales. The materials design starts from the surrounding structure of the rare-earth ions in atomic scale. For live cell imaging, the requirement of the particle size is in the nanometre scale between 20 and 200 nm. For giving biocompatibility, surface modification of the particles with biofunctional polymers also in nanometre scale. The size of the cells is generally in micrometre scale as the case of erythrocyte with about 10 μm. The imaging of the live body is conducted mainly in between millimetre and metre scales. For the entire new NIR-FBI system will be a fruit of the collaboration of the technologies in various scales. The size of the RED-CNP itself varies from several tens nanometre size to micrometre size according to the application.

In this paper, the development of NIR-FBI systems is reviewed as an example of the 'polyscale technologies.' The development starts from the design and preparation of the RED-CNP proceeding to the surface modification of the RED-CNP with polymers with biological functions, and terminates at the imaging of biological substances with a particularly designed imaging system.

Design and preparation of RED-CNP

The RED-CNP are known to emit not only NIR light but visible light under the NIR excitation. The latter emission is called infrared to visible upconversion (UC) emission. Figure 1 illustrates the excitation scheme of erbium (Er) ions doped in a host. The UC emission occurs due to the stepwise excitation of the 4f electron system. The use of the UC emission for the FBI was proposed in late 1990s.[3–11] The authors have proposed to use erbium doped yttrium oxide (Y_2O_3 : Er) nanoparticles for the UC-FBI and YPO_4 : Er nanoparticles for the NIR-FBI. The UC-FBI is attractive for the use of currently used CCD for visible light under the NIR excitation, though the quantum efficiency of the UC emission is comparably smaller than the NIR-FBI case due to the stepwise excitation of the system. On the other hand, the NIR emission by the NIR excitation is efficient since the excitation is only a single step. In the case of the Er, it can emit very efficient emission at 1550 nm under 980 nm excitation, which is practically used for the optical fibre amplifier for optical communications.[1] The observation in the NIR wavelength region is also attractive for the weak scattering of the emitted light from the probe. However, CCD that can detect 1550 nm light is not well available. InGaAs CCD can detect the light with wide wavelength range in the NIR regrion, though the InGaAs CCDs are much less produced than silicon CCDs and the sensitivity and resolution of them are not as high as those of the silicon CCDs. Accordingly, the UC-FBI system is the technology to be used immediately by changing the excitation light into the NIR laser diode, while the NIR-FBI is future oriented technology with less scattering and higher emission efficiency by introducing the NIR CCD. The material design, as an atomic technology, for the UC and NIR-FBI probes are different. As shown in Fig. 1, for the UC emission, the lifetime of the level labelled as 10 253 cm^{-1} should be long to excite the system into the upper level (20 530 cm^{-1}) by the second step excitation. The host should be selected to retain the 1 0253 cm^{-1} level for a long time as shown in Fig. 1*b*. In contrast, for the NIR emission at 1550 nm, the lifetime of the 10 253 cm^{-1} level should be shorter to relax into the 6591 cm^{-1} level so that one can obtain an efficient emission from the 6591 cm^{-1} level by avoiding the above UC process. The above scheme is an example of the need of the atomic scale design of the RED-CNP.[12]

Preparation of size controlled RED-CNP

The next step from the above atomic scale design is the preparation of the RED-CNP under the size control. The size of the particles should be in between 10 and 200 nm for a sufficient emission intensity and dispersion in physiological solutions. An example of the preparation route for the RED-CNP is the use of homogeneous decomposition of urea for precursor precipitation to prepare the Y_2O_3 : Er nanoparticles. Figure 2 shows the particles prepared by the method. The precursor, $YCO_3(OH)$, was precipitated from the starting solution with yttrium and erbium nitrate by adding the urea. At the room temperature, one can homogeneously diffuse the urea without any precipitation. When the solution is heated up to 80°C, the urea decomposes into a carbonate ion and ammonium ion to induce hydroxyl ion, which work as precipitant of the precursors. Due to the homogeneous distribution of the precipitant, the authors could form the precursor with a narrow size distribution. Figure 2 compares the Y_2O_3 : Er nanoparticles prepared by an usual alkali precipitation method and the homogeneous precipitation method. The particle size distribution is obviously narrower with the homogeneous precipitation method. The Y_2O_3 : Er can

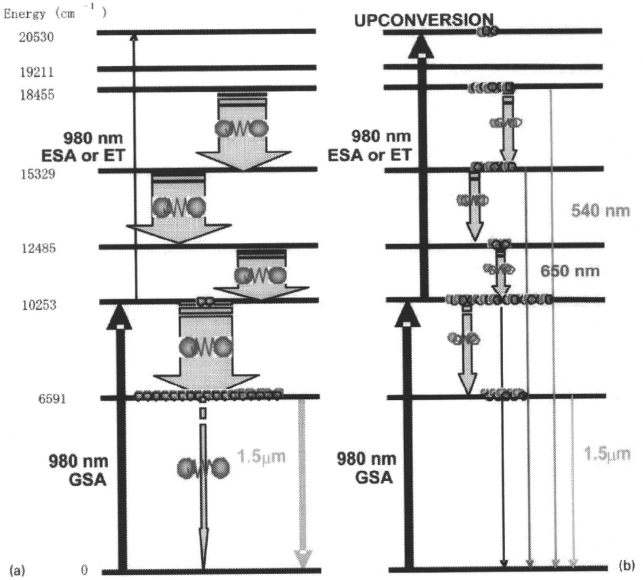

a ideal scheme for 1·5 μm emission; *b* ideal scheme for upconversion emission

1 Schematic diagram of the excitation and emission schemes of Er^{3+} ions under 980 nm excitation

be obtained by calcinate the precursor at 900°C for 1 h. Figure 3 shows the upconversion spectrum from the Y_2O_3:Er by the homogeneous precipitation.

Surface modification of RED-CNP by polymers

The RED-CNP is easy to be agglomerated in physiological solutions because of their large specific surface area due to the small particle size. To prevent the agglomeration of the particles, a steric repulsion by a polymer should be introduced to the particles. The necessity of the surface modification is not only because of the dispersion, but for giving specific interaction of the particles with biological substances. Poly(ethylene glycol) (PEG) is known to have the dispersion effects to be modified on the inorganic particles.[13–25] The PEG chains are also known to prevent non-specific adsorption to the general substances in live body. Acetal-PEG-block poly [2-(N,N-dimethylamino)ethylmethacrylate]

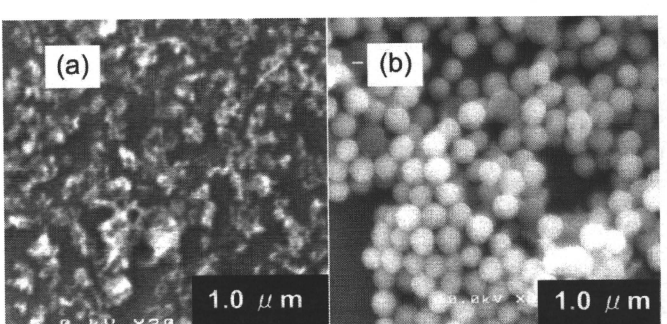

2 Images (FESEM) of precursors obtained by *a* conventional carbonate precipitation method and *b* homogeneous precipitation methods

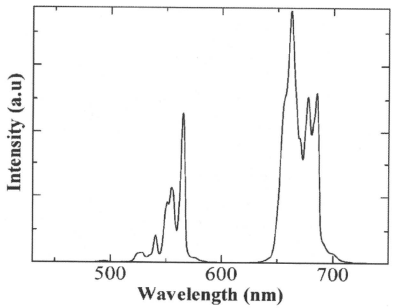

3 Typical upconversion spectrum of Er^{3+} in Y_2O_3 nanoparticles

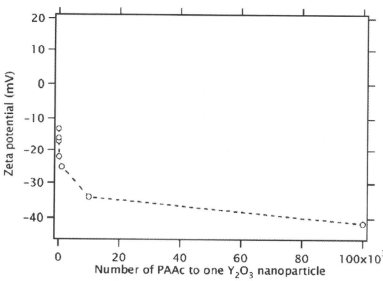

4 Zeta potential of Y_2O_3 nanoparticles as function of number PAAc in solution

(Acetal-PEG-*b*-PAMA) can be utilised for an installation of ligand moiety, such as biotin, with adsorption to a targeting protein by a specific ligand-receptor interaction.[26,27] The PAMA part has positive charge to interact with the surface of the ionic solids. The surface of the Y_2O_3:Er particles is known to be positively charged. For interacting those two positively charged parts, the authors used poly (acrylic acid) (PAAc) as an interfacing agent. By this method, the acetal-PEG-*b*-PAMA is reported to be firmly adsorbed on the surface the Y_2O_3 particles even under the three times centrifugal washes.[28,29] The precise experimental conditions for the

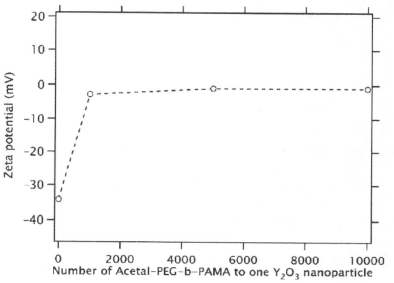

5 Zeta potential of Y_2O_3 nanoparticles as function of number of acetal-PEG-*b*-PAMA addition to colloidal solution

surface modification is described in the literature. Figures 4 and 5 show the zeta potential of the particles after PAAc and acetal-PEG-*b*-PAMA modification. The potential once moved into negative by the modification with the PAAc and recovered to be neutral by the post-modification with the acetal-PEG-*b*-PAMA. The particles are successfully modified by the double layer of the PAAc and Acetal-PEG-*b*-PAMA polymers. The firm modification was also confirmed using Fourier transform infrared spectroscopy.

Design and development of FBI system under NIR excitation

The authors developed a biological microimaging system with the NIR excitation. Figure 6 shows the demonstrative work of the system by imaging the macrophages incorporated with the Y_2O_3:Er nanoparticles. The modified particles were then introduced into macrophage cells totally by 44 h incubation. In Fig. 6, the bright filed image and the UC image of the macrophages are shown. The authors could successfully achieve the UC cell imaging using the NIR-FBI system. The developed system also is equipped with an NIR CCD. Figure 7 shows the images of the YPO_4:Er particles observed with the NIR CCD together with the emission spectrum under the 980 nm excitation. Bright fluorescence at 1550 nm was observed in the view of the microscope. It implies that the YPO_4:Er particles are potential candidate material for the NIR imaging using the developed system.

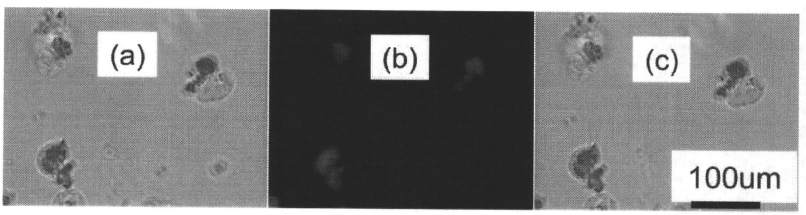

a bright field image; *b* UC image; *c* merged image

6 Englobement of Y_2O_3:Er nanoparticles by macrophage cells

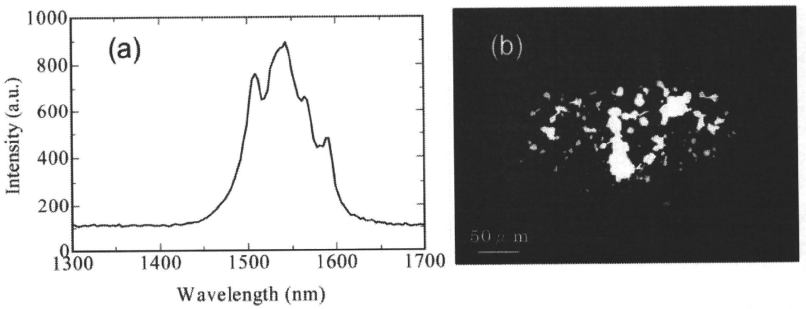

7 ***a*** **emission spectrum and** ***b*** **NIR image from YPO_4:Er particles**

Summary

The UC-FBI and NIR-FBI were demonstrated as bioimaging under the NIR excitation. The demonstration was achieved by an atomic scale design of the RED-CNP, nanoscale processing of the RED-CNP, nanoscale surface modification of functional polymers and microscale observation of the cells. The hole process for the imaging can be called as an example of 'polyscale technology'.

Acknowledgements

This work was supported by 'Academic Frontier' Project for Private Universities: Matching Fund Subsidy from Ministry of Education, Culture, Sports, Science and Technology (MEXT), 2006–2010 and 'Development of upconversinon nano-particles for bio-nano-photonics' in 2005–2007 from New Energy and Industrial Technology Development Organization (NEDO) of Japan.

References

1. S. Sudo: 'Optical fiber amplifiers: materials, devices, and applications'; 1997, Norwood, MA, Artech House Publishers.
2. R. C. Powell: 'Physics of solid state laser materials'; 1998, New York, Springer.
3. H. J. M. A. A. Zijlmans, J. Bonnet, J. Burton, K. Kardos, T. Vail, R. S. Niedbala and H. J. Tanke: *Anal. Biochem.*, 1999, **267**, 30–36.
4. P. Corstjens M. Zuiderwijk, A. Brink, S. Li, H. Feindt, R. S. Neidbala and H. Tanke: *Clin. Chem.*, 2001, **47**, 1885–1893.
5. F. van de Rijke, H. Zijlmans, S. Li, T. Vail, A. K. Raap, R. S. Niedbala and H. J. Tanke: *Nat. Biotechnol.*, 2001, **19**, 273–276.
6. J. Hampl, M. Hall, N. A. Mufti, Y. M. M. Yao, D. B. MacQueen, W. H. Wright and D. E. Cooper: *Anal. Biochem.*, 2001, **288**, 176–187.
7. R. S. Niedbala, H. Feindt, K. Kardos, T. Vail, J. Burton, B. Bielska, S. Li, D. Milunic, P. Bourdelle and R. Vallejo: *Anal. Biochem.*, 2001, **293**, 22–33.
8. K. Kuningas, T. Ukonaho, H. Päkkilä, T. Rantanen, J. Rosenberg, T. Lövgren and T. Soukka: *Anal. Chem.*, 2006, **76**, 4690–4696.
9. C. G. Morgan and A. C. Mitchell: *Biosensors Bioelectron.*, 2007, **22**, 1769–1775.
10. L. Wang, R. Yan, Z. Huo, L. Wang, J. Zeng, J. Bao, X. Wang, Q. Peng and Y. Li: *Angew. Chem. Int. Ed.*, 2005, **44**, 6054–6057.
11. C. G. Morgan, S. Dad and A. C. Mitchell: 'Present status of, and prospects for, upconverting phosphors in proximity-based bioassay', *J. Alloys Compd*, 2008, **451**, 526–529.
12. K. Soga, W. Wang, R. E. Riman, J. B. Brown and K. R. Mikeska: *J. Appl. Phys.*, 2003, **93**, 2946–2951.
13. S. Sivakumar, P. R. Diamente and F. C. van Veggel: *Chem. Eur. J.*, 2006, **12**, 5878–5884.
14. P. R. Diamente, R. D. Burke and F. C. J. M. van Veggel: *Langmuir*, 2006, **22**, 1782–1788.
15. P. R. Diamente and F. C. J. M. van Veggel: *J. Fluoresc.*, 2005, **15**, 543–551.
16. S. F. Lim, R. Riehn, W. S. Ryu, N. Khanarian, C.-K. Tung, D. Tank and R. H. Austin: *Nano Lett.*, 2006, **6**, 169–174.
17. C. Woghire, B. Sharma and S. Stein: *Bioconjugate Chem.*, 1993, **4**, 314–318.
18. H. F. Gaertner and R. E. Offord: *Bioconjugate Chem.*, 1996, **7**, 38–44.
19. Y. Akiyama, H. Otsuka, Y. Nagasaki, M. Kato and K. Kataoka: *Bioconjugate Chem.*, 2000, **11**, 947–950.
20. S. Zhang: *React. Funct. Polym.* 2003, **56**, 17–25
21. F. M. Veronese: *Biomaterials*, 2001, **22**, 405–417.
22. M. J. Roberts, M. D. Bentley, J. M. Harris: *Adv. Drug Delivery Rev.*, 2002, **54**, 459–476.
23. H. Otsuka, Y. Nagasaki and K. Kataoka: *Adv. Drug Delivery Rev.*, 2003, **55**, 403–419.
24. P. Caliceti: *J. Controlled Release*, 2002, **83**, 97–108.
25. R. B. Greenwald, Y. H. Choe, J. McGuire and C. D. Conover: *Adv. Drug Delivery Rev.*, 2003, **55**, 217–250.
26. T. Ishii, H. Otsuka, K. Kataoka and Y. Nagasaki: *Langmuir*, 2004, **20**, 561–564.
27. Y. Nagasaki, T. Ishii, Y. Sunaga, Y. Watanabe, H. Otsuka and K. Ka-taoka: *Langmuir*, 2004, **20**, 6396–6400.
28. K. Soga, R. Koizumi, M. Yamada, D. Matsuura and Y. Nagasaki: *J. Photopolym. Sci. Tech.*, 2005, **18**, 73–74.
29. T. Konishi, K. Shimizu, Y. Saito and K. Soga: *J. Photopolym. Sci. Tech.*, 2007, **20**, 11–15.

Organic-ligand-assisted hydrothermal synthesis of ultrafine and hydrophobic ZnO nanoparticles

Tahereh Mousavand, Satoshi Ohara, Takashi Naka, Mitsuo Umetsu, and Seiichi Takami
Institute of Multidisciplinary Research for Advanced Materials, Tohoku University, 2-1-1 Katahira, Aoba-ku, Sendai 980-8577, Japan

Tadafumi Adschiri[a)]
WPI, Advanced Institute for Materials Research, Tohoku University, 2-1-1 Katahira, Aoba-ku, Sendai 980-8577, Japan

(Received 9 June 2009; accepted 8 September 2009)

In this study, we report the synthesis of uniform and narrowly size-distributed ZnO nanoparticles with sizes of approximately 3 nm; the nanoparticles were prepared by means of organic-ligand-assisted hydrothermal conditions with various organic modifiers. The results obtained herein revealed that among the various functional groups tested (alcohols, aldehydes, carboxylic acids, and amines), only hexanol effectively controlled the nucleation and crystal growth of spherical ZnO nanoparticles. The use of hexanol also caused the surface of the ZnO particles to change from hydrophilic to hydrophobic, which would enhance the dispersion of these particles in polymer matrices, paints, cosmetics, and other organic application media.

I. INTRODUCTION

ZnO nanoparticles are used in many applications such as paints, sunscreens, varnishes, plastics, cosmetics, and polymer matrices.[1–7] The dispersion media used in such applications are hydrophobic, whereas the inorganic nanoparticles possess a hydrophilic tendency. Therefore, simple mixing of the nanoparticles in these media causes a nonhomogeneous dispersion of nanoparticles, as well as nanoparticle aggregation. This problem can be resolved by functionalizing the surfaces of the inorganic nanoparticles so that they are compatible with the application media. Thus, properly tailoring the surface of these ZnO nanoparticles strongly influences their homogeneous distribution and perfect dispersion in organic media, and the hydrophilicity of ZnO nanoparticles are changed by in situ[8,9] or post-surface modifications.[1,10]

Furthermore, the size of the particles also influences the transparency of application media.[1] Therefore, many researchers have attempted to control the size and morphology of ZnO nanoparticles.[7,11–14] Reducing the particle size of ZnO down to less than 10 nm with a high production rate, namely not at a dilute concentration, has been considered difficult. This is mainly due to the high solubility of ZnO in aqueous solutions even at a low temperature range, which leads to the growth of particles.

Recently, we proposed a new method of one-pot synthesis of organic modified metal oxide nanoparticles by using supercritical water as a reaction media.[15–19] In this study, we applied this supercritical hydrothermal synthesis method for synthesizing surface modified ZnO nanoparticles by using functional groups such as alcohols. This method is advantageous relative to the previous ZnO modification methods[1,8–10] because it produces hydrophobic, spherical particles smaller than 3 nm with narrowly size distribution.

II. EXPERIMENTAL METHOD

Pressure resistance tube reactors composed of SUS 316 with an inner volume of 5.0 mL were used for hydrothermal synthesis. The reactor was loaded with 2.5 mL of an aqueous solution of 0.1 M $Zn(NO_3)_2$ and 0.2 M KOH as starting material. To modify the surface of ZnO nanoparticles, 0.1 mL of surface modifier (C_6–OH, C_5–CHO, C_5–COOH, and C_6–NH_2) was added to the starting material. The reactors were then capped tightly and placed into an electric furnace and the temperature was maintained at 200 °C. The reaction was allowed to proceed for 10 min and was subsequently terminated by submerging and quenching the reactor in a water bath. Reactions were carried out at 1.6 MPa at 200 °C. After quenching, products were recovered by distillated water for nonmodified particles and ethanol for modified products. The nanoparticles were then purified by three cycles of centrifugation/decantation using ethanol and water for modified and nonmodified particles, respectively. Finally, the products were dried in vacuum, overnight.

The products were analyzed by x-ray diffractometry (XRD) and the XRD data were measured on a Dmax

[a)]Address all correspondence to this author.
e-mail: ajiri@tagen.tohoku.ac.jp
DOI: 10.1557/JMR.2010.0037

γ_n x-ray diffractometer (Rigaku, Tokyo, Japan) with Cu K_α radiation. The size and morphology of ZnO particles were observed with transmission electron microscopy (TEM; JEM-1200 EX II, JEOL, Ltd., Tokyo, Japan). For analyzing the organic molecules contained in the products, attenuated total reflectance Fourier transform infrared (FTIR) spectra were measured with an FTIR-680 plus spectrometer (Jasco, Tokyo, Japan) at a resolution of 4 cm^{-1}. Thermogravimetric analysis (TGA) was performed by a Thermo Plus (Rigaku) under a constant flow of argon gas at a heating rate of 10 °C/min.

III. RESULTS AND DISCUSSION

Figure 1 shows the XRD patterns of hydrothermal synthesized ZnO nanoparticles without and with various modifiers and standard ZnO crystals with the hexagonal wurtzite structure (JCPDS Card No. 36-1451, $a = 3.250$, $c = 5.207$). Modified with hexylamine and hexanol, particle samples had the ZnO structure without any extra by-products. On the other hand, the patterns of samples synthesized with hexaldehyde and carboxylic acid showed that the ZnO structure did not form. This phenomenon was probably due to differences of pH among the aqueous solutions containing the various modifiers. In the case of acidic modifiers, R–COOH and R–CHO, ZnO nanoparticles seem to dissolve into the solution, consequently, other crystallographic phases, such as $Zn(OH)_2$, was stabilized, as shown in Fig. 1(e). However, in the neutral and base condition the pure phase of ZnO was formed. The size, morphology, and distribution of nanoparticles can be controlled by adjusting reaction temperature, pressure, and functional additives in hydrothermal synthesis near the critical point of water.

Figures 2(a)–2(d) show the TEM images of the samples synthesized under hydrothermal conditions. As shown in Fig. 2(a), when modifiers were not added to the starting material, inhomogeneous particles were formed. These particles were small with an aspect ratio of 1.1; rods with an aspect ratio of 4.4 (mean size: 200 nm × 45 nm) were also present.

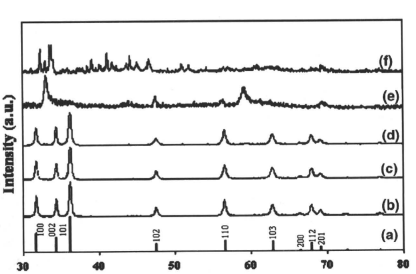

FIG. 1. XRD spectra of (a) standard ZnO, (b) ZnO nanoparticles synthesized without modifier, and ZnO nanoparticles modified with (c) R–NH_2, (d) R–OH, (e) R–CHO, and (f) R–COOH at 200 °C.

The rates of nucleation and crystal growth seem to vary with pH, as pointed out previously,[7,13,14] i.e., when the pH is high, the nucleation rate is high, and nanoparticles form at a faster rate. Figure 2(b) shows irregular ZnO particles produced from a solution of starting materials with the addition of the amine modifier. It is consistent with this proposed nucleation scheme that an average size was reduced to 85 nm with a narrowly size distribution. The observed size distribution and larger aspect ratio were probably caused by Ostwald ripening,[20] facilitated probably when the pH of reaction media is lower under subcritical conditions, in other words, the solubility of ZnO_2 is higher.

However, as shown in Fig. 2(c), in the case of the R–OH modifier, the crystal dimension was reduced considerably (16 ± 1.3 nm) with a narrowly size distribution. The size of these particles as calculated from their XRD pattern was estimated to be 17 nm, which agreed well with the mean size estimated from the TEM image. Figure 2(d) indicates that the size of ZnO particles prepared with R–OH decreased to 2.8 ± 0.6 nm when the molar ratio [moles of modifier (R–OH)/moles of starting material] was increased. The morphology changes to spherical. In addition to the slower nucleation promoted under higher pH conditions, the crystal growth was suppressed by the surface modifier under the hydrothermal condition, as mentioned later.

The chemical interactions between the surfaces of the inorganic nanoparticles and functional modifiers of R–OH and R–NH_2 were investigated by means of FTIR analysis. In Figs. 3(a) and 3(b) there are three spectra corresponding to bare ZnO, modified ZnO nanoparticles, and the organic reagents. In Fig. 3(a), the appearance of absorption peaks in the modified ZnO spectrum that are not presented in bare ZnO spectrum demonstrates that the surface properties of the modified nanoparticles were changed by the addition of R–OH to the starting materials. The absorption peaks at 2922 and 2857 cm^{-1} correspond to CH_2 and CH_3 stretching vibrations, respectively, whereas the peaks at 1058 and 1419 cm^{-1} correspond to C–O and C–H bending vibrations, respectively. These results prove that the inorganic ZnO nanoparticles' surface effectively changed from hydrophilic (owing to the presence of OH groups on the surface of ZnO nanoparticles) to hydrophobic. Furthermore, the observed C–O bond perhaps resulted from covalent bonding between OH on the surface of ZnO and the R–OH modifier. In contrast, the absorption peak at 3380 cm^{-1} is characteristic of O–H bonding. This peak likely indicates that not only chemical interactions but also physical adsorption took place. Figure 3(b) shows the spectra of ZnO nanoparticles modified with the amine groups. In this case, the spectrum of the modified ZnO nanoparticles has the

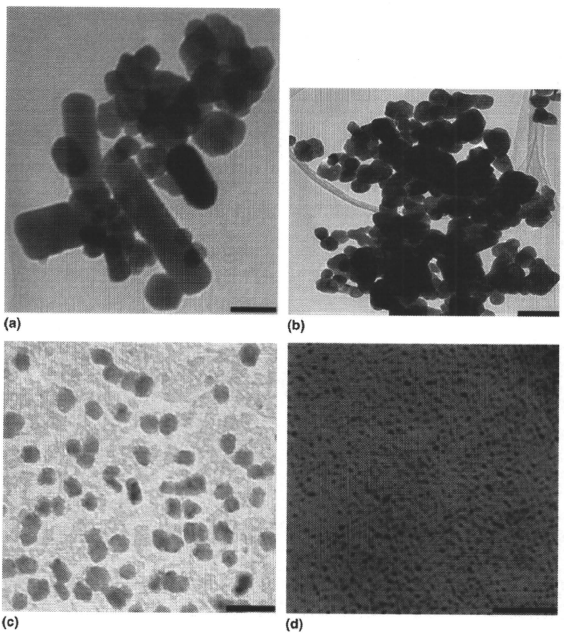

FIG. 2. TEM images of ZnO nanoparticles synthesized at 200 °C (a) without modifier and modified with (b) R–NH_2, (c) R–OH (molar ratio = 8.0), and (d) R–OH (molar ratio = 800).

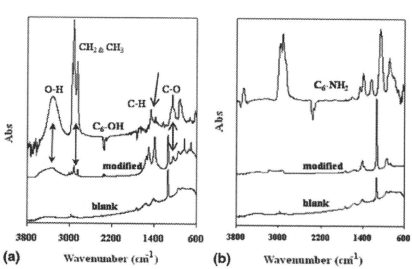

FIG. 3. FTIR spectra of ZnO nanoparticles synthesized at 200 °C with (a) R–OH and (b) R–NH_2 modifiers.

same features as those in the bare ZnO spectrum. This fact suggests that the amine groups cannot be used as an effective surface modifier for ZnO particles.

These observations in the FTIR analysis were reconfirmed by TGA, since the weight loss can result from the dissociation and/or desorption of organic modifiers from the inorganic surfaces at certain high temperatures. The dissociation temperature reflects the strength of bonding between the inorganic surface and the modifier. Figure 4 displays the thermogravimetric weight loss of samples synthesized with the modifiers, as well as that of nonmodified ZnO nanoparticles. The weight loss observed for the nonmodified particles [line (a)] and for the particles modified with R–NH_2 [line (b)] are similar in appearance; both lines correspond to the release of water molecules from the surface and the inside of the crystal of ZnO. However, for the sample modified with R–OH [line (c)], a large weight reduction was observed. Line (c) features three slopes. At the first stage (first slope), hydroxyl groups at the surface of the particles are released. The second stage of mass loss (second slope between 157 and 250 °C) perhaps corresponded to the loss of physisorbed or adsorbed modifiers at the surface of the particles, as was suggested by the FTIR results. Finally, the last slope between 300 and 430 °C might be attributed to the dissociation of the organic modifier,

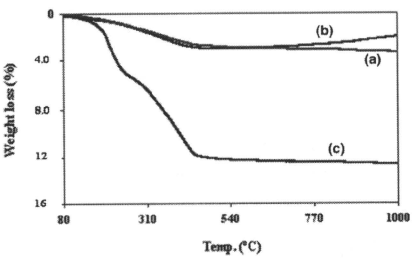

FIG. 4. Thermogravimetric weight loss of ZnO nanoparticles synthesized at 200 °C (a) without modifier and modified with (b) R–NH_2 and (c) R–OH.

which seemed to be of a covalently bound to the surface of the ZnO nanoparticles. These features on the TGA analysis were consistent with the results of FTIR analysis shown in Fig. 3.

The reason why the surface modification by amines was not successful can be explained by elucidating the mechanism of reaction. Under the conditions used here, two important factors influence the reaction between the organic modifiers and the surface of the inorganic particles.[21] The first factor is the surface charge of metal oxide nanoparticles, and the second one is the dissociation constant of the modifiers. The isoelectric point of ZnO is about 9.4; the surface charge of nanoparticles at a pH lower and higher than this value is positive (protonated) and negative (deprotonated), respectively. On the other hand, the pKa of the hexylamine modifier used in this work is 10.56, and at a pH less than this value, amine groups dissociate, namely, R–NH_3^+ appear in the reaction media. However, under hydrothermal condition, pH < 11 is expected owing to promoting the miscibility of R–NH_2 with water. In this situation, dissociation of amine groups does not take place. Consequently, no chemical reaction, in other words, no adsorption of the amine modifiers is expected to occur on the inorganic nanoparticles since both the surfaces and the modifiers are negatively charged.

However, when R–OH (pKa = 7.46) was loaded with ZnO nanoparticles, the ZnO particle's surface changed from hydrophilic to hydrophobic. In this situation, two types of bonding occurred: (i) covalent bonding between the positive surface charge of ZnO(OH_2^+) and the dissociated part of the R–OH modifier and (ii) adsorption caused by affinity between OH groups on the particles' surface and OH of alcohol groups of the R–OH modifier negatively charged. Thus, we concluded that R–OH, unlike R–NH_2, affectively inhibited crystal growth on the ZnO nanoparticles. Therefore, we demonstrated that the chemical properties of the modifier affect strongly not only the size but also the efficiency of the surface modification on ZnO nanoparticles. In this study, alcohol groups are the best organic reagent for in situ surface modification of ZnO nanoparticles.

IV. CONCLUSIONS

In conclusion, organic-ligand-assisted hydrothermal synthesis of ZnO nanoparticles using appropriate modifiers under hydrothermal conditions near the critical point resulted in the formation of uniform and narrowly size-distributed nanoparticles with 2.8 nm in diameter. Among the different functional groups tested here, including alcohols, aldehydes, carboxylic acids, and amines, only R–OH could be attached stably on the ZnO surface and reduce the size. In this case, successfully, the nanoparticles' surface is converted from hydrophilic to hydrophobic. The FTIR and TGA results obtained herein confirmed that hexanol strongly influenced the surface properties of ZnO particles through direct bonding at the particles' surface. We believe that control of these aspects strongly affects the homogeneous dispersion of ZnO nanoparticles, which is an important feature, therefore, applicable for producing paints, cosmetics, and hybrid materials with polymer matrices or organic media.

ACKNOWLEDGMENTS

This work was supported by a Scientific Research Grant from the Ministry of Education, Science, Sports, and Culture of Japan. This research was also partly supported by a Grant-in-Aid for the COE project, Giant Molecules and Complex System (TM).

REFERENCES

1. V. Khrenov, M. Klapper, M. Koch, and K. Müllen: Surface functionalized ZnO particles designed for the use in transparent nanocomposites. *Macromol. Chem. Phys.* **206,** 95 (2005).
2. U. Pal and P. Santiago: Controlling the morphology of ZnO nanostructures in a low-temperature hydrothermal process. *J. Phys. Chem. B* **109,** 15317 (2005).
3. H. Kim and W. Sigmund: ZnO nanocrystals synthesized by physical vapor desposition. *J. Nanosci. Nanotechnol.* **4**(3), 275 (2004).
4. R. Viswanathan and R.B. Gupta: Formation of zinc oxide nanoparticles in supercritical water. *J. Supercrit. Fluids* **27,** 187 (2003).
5. R. D. Laundon: Synthesis of ZnO particles. U.S. Patent No. 5 876 688, March 2, 1999.
6. H. Althues, P. Simon, F. Philipp, and S. Kaskel: Integration of zinc oxide nanoparticles into transparent poly(butanediolmonoacrylate) via photopolymerization. *J. Nanosci. Nanotechnol.* **6,** 409 (2006).
7. H. Zhang, D. Yang, Y. Ji, X. Ma, J. Xu, and D. Que: Low temperature synthesis of flowerlike ZnO nanostructures by cetyltrimethylammonium bromide-assisted hydrothermal process. *J. Phys. Chem. B* **108**(13), 3955 (2004).
8. Y-L. Wu, A.I.Y. Tok, F.Y.C. Boey, X.T. Zeng, and X.H. Zhang: Surface modification of ZnO nanocrystals. *Appl. Surf. Sci.* **253,** 5473 (2007).

9. L. Tang, B. Zhou, Y. Tian, F. Sun, Y. Li, and Z. Wang: Synthesis and surface hydrophobic functionalization of ZnO nanocrystals via a facile one-step solution method. *Chem. Eng. J.* **139,** 642 (2008).
10. R. Hong, T. Pan, J. Qian, and H. Li: Synthesis and surface modification of ZnO nanoparticles. *Chem. Eng. J.* **119,** 71 (2006).
11. P. Singh, A. Kumar, A. Kaushal, D. Kaur, A. Pandey, and R.N. Goyal: Influence of minor elements additions on microstructure and properties of 93W-4·9Ni-2·1Fe alloys. *Bull. Mater. Sci.* **31,** 573 (2008).
12. S. Ohara, T. Mousavand, M. Umetsu, S. Takami, T. Adschiri, Y. Kuroki, and M. Takata: Hydrothermal synthesis of fine zinc oxide particles under supercritical conditions. *Solid State Ionics* **172,** 261 (2004).
13. K. Sue, K. Kimura, K. Murata, and K. Arai: Effect of cations and anions on properties of zinc oxide particles synthesized in supercritical water. *J. Supercrit. Fluids* **30,** 325 (2004).
14. B. Liu and H.C. Zeng: Hydrothermal synthesis of ZnO nanorods in the diameter regime of 50 nm. *J. Am. Chem. Soc.* **125,** 4430 (2003).
15. T. Mousavand, S. Takami, M. Umetsu, S. Ohara, and T. Adschiri: Supercritical hydrothermal synthesis of organic-inorganic hybrid nanoparticles. *J. Mater. Sci.* **41,** 1445 (2006).
16. S. Ohara, T. Mousavand, T. Sasaki, M. Umetsu, T. Naka and T. Adschiri: Continuous production of fine zinc oxide nanorods by hydrothermal synthesis in supercritical water. *J. Mater. Sci.* **43,** 2393 (2008).
17. J. Zhang, S. Ohara, M. Umetsu, T. Naka, T.Y. Hatakeyama, and T. Adschiri: Colloidal ceria nanocrystals: A tailor-made crystal morphology in supercritical water. *Adv. Mater.* **19,** 203 (2007).
18. T. Mousavand, S. Ohara, M. Umetsu, J. Zhang, S. Takami, T. Naka, and T. Adschiri: Hydrothermal synthesis and in situ surface modification of boehmite nanoparticles in supercritical water. *J. Supercrit. Fluids* **40,** 397 (2007).
19. T. Mousavand, J. Zhang, S. Ohara, M. Umetsu, T. Naka, and T. Adschiri: Organic-ligand-assisted supercritical hydrothermal synthesis of titanium oxide nanocrystals leading to perfectly dispersed titanium oxide nanoparticle in organic phase. *J. Nanopart. Res.* **6,** 1067 (2007).
20. J.A. Marqusee and J. Ross: Kinetics of phase transitions: Theory of Ostwald ripening. *J. Chem. Phys.* **79,** 373 (1983).
21. T. Mousavand, T. Naka, S. Ohara, and T. Adschiri: Optimization and reaction mechanism of in situ surface modification of metal oxide nanoparticles. (in preparation).

J|A|C|S
COMMUNICATIONS

Published on Web 02/03/2010

Selective Growth of Monoclinic and Tetragonal Zirconia Nanocrystals

Kazuyoshi Sato,* Hiroya Abe, and Satoshi Ohara

Joining and Welding Research Institute, Osaka University, 11-1 Mihogaoka, Ibaraki, Osaka 567-0047 Japan

Received December 19, 2009; E-mail: k-sato@jwri.osaka-u.ac.jp

In this communication, we demonstrate for the first time a selective growth of single-crystalline pure monoclinic and tetragonal ZrO_2 nanocrystals of <10 nm diameter, driven by controlling their surface energy. The growth of metal oxide nanocrystals with a well-organized crystalline phase is of fundamental and technological interest because in this way it is possible to tune their size-dependent unique properties,[1,2] and thus establish their potential application in chemistry, electronics, optics, magnetics, and mechanics. ZrO_2 is a case in point, with a phase-dependent potential application in a number of technologies. Monoclinic ZrO_2 is important for catalysis,[3] gate dielectrics,[4] and bioactive coatings on bone implants,[5] while tetragonal and cubic ZrO_2 are promising candidates for fuel cell electrolytes,[6] oxygen sensors,[7] and phase-transformation-toughened structural materials.[8]

In particular, the growth of pure monoclinic ZrO_2 nanocrystals of <10 nm diameter is a challenging task in the selective growth of the different phases, since a high-temperature tetragonal phase is stable at room temperature as the consequence of the dominance of the surface energy contribution to the Gibbs free energy of formation in this size range.[9] A report by Zhang et al. suggests that the surface energy of oxides can be controlled by capping the surface with an organic substance.[10] They successfully grow the unstable (001) faceted CeO_2 by capping with decanoic acid. Although surface capping-assisted growth using similar anionic substances was also applied to ZrO_2, the resulting nanocrystals of <10 nm diameter still chiefly exhibited a tetragonal phase.[11,12] Herein, we report the facile selective growth route of pure monoclinic and tetragonal ZrO_2 nanocrystals of <10 nm diameter, with and without a cationic capping agent, $N(CH_3)_4^+$.

In a typical procedure, a Zr^{4+} precursor ($ZrOCl_2 \cdot 8H_2O$, 0.01 mol) was dissolved in a basic aqueous solution (pH ≈ 10.5) containing a mixture of either $N(CH_3)_4HCO_3$ (tetramethyl-ammonium hydrogen carbonate; TMAHC)/$N(CH_3)_4OH$ (tetramethyl-ammonium hydroxide; TMAH) or $KHCO_3$/KOH. The clear solution of dissolved precursor was transferred into a 50 mL, Teflon-lined, stainless steel autoclave and heat treated at 150 °C. The products were obtained as well-dispersed colloidal solutions. ZrO_2 nanocrystals in the solution were purified by washing ten times with deionized water using ultrafiltration, with a molecular weight cutoff of 3000 for subsequent characterizations. The yield of ZrO_2 nanocrystals was almost 100% in both TMAHC/TMAH and $KHCO_3$/KOH systems. The ZrO_2 nanocrystals were characterized by transmission electron microscopy (TEM; JEOL JEM-2100F) with an accelerating voltage of 200 kV, X-ray diffraction (XRD; JEOL JDX-3530M) with Cu Kα radiation ($\lambda = 0.154178$ nm) at 40 kV and 40 mA, Raman spectroscopy (Horiba Jobin Yvon LabRAM ARAMIS) at room temperature with 532 nm excitation line of an diode-pumped solid state laser, and UV−vis adsorption spectroscopy (Shimadzu, UV-2450) with a double-beam recording spectrometer using 1 cm quartz cells.

Figure 1 shows TEM images of ZrO_2 nanocrystals grown in the TMAHC/TMAH and $KHCO_3$/KOH systems. These images clearly

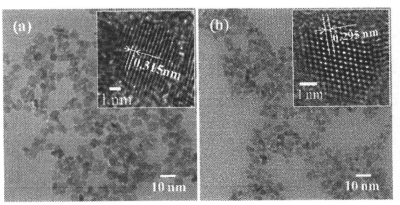

Figure 1. TEM images of ZrO_2 nanocrystals grown in the (a) TMAHC/TMAH and the (b) $KHCO_3$/KOH systems. Each respective inset shows an HRTEM image of an isolated nanocrystal.

indicate that both nanocrystals consist entirely of crystals of a uniform size of <10 nm diameter. The inset shows the high-resolution TEM (HRTEM) image of an isolated nanocrystal, indicating the single-crystalline nature of the nanocrystals grown in both systems. The lattice spacing is 0.315 and 0.295 nm, corresponding to (−111) of monoclinic and (111) of tetragonal ZrO_2 for the nanocrystals grown in the TMAHC/TMAH and the $KHCO_3$/KOH systems, respectively. Figure S-1 (Supporting Information) shows the size distribution of the ZrO_2 nanocrystals in the aqueous solution measured by dynamic light-scattering method, showing the nanocrystals almost perfectly dispersed in the aqueous solution by taking into account that the hydrodynamic diameter overestimates by several nanometers the real size.[13]

The XRD patterns of the powdered nanocrystals shown in Figure 2 further confirm that the respective phases observed in the HRTEM images represent the entire nanocrystals in both systems. The peaks are relatively broad, supporting the very small crystalline size. The sizes estimated by Scherrer's formula using full width of half maxima of (−111) for monoclinic and (111) for tetragonal phases were almost the same at 5.4 and 5.2 nm, respectively. The inset of Figure 2 shows the Raman spectra recorded for colloidal solutions of ZrO_2 nanocrystals. For the nanocrystals grown in the TMAHC/TMAH system, the purely monoclinic structure is confirmed by the observation of 13 Raman modes of the 18 ($9A_{1g} + 9B_{1g}$) expected by symmetry analysis,[14] which provides evidence that the growth of monoclinic ZrO_2 nanocrystals shown above was driven by the surface capping with $N(CH_3)_4^+$ (denoted as TMA^+ in the following text), and not by the surface energy reduction through agglomeration by drying. The broad Raman band for the tetragonal ZrO_2 nanocrystals indicates that they involve highly disordered lattice defects.[14]

Optical absorption spectra of the colloidal ZrO_2 solutions shown in Figure 3 provide information relating to the lattice defects. Two absorption shoulders are clearly observed at around 5.2 and 5.7 eV for the ZrO_2 nanocrystals grown in the TMAHC/TMAH system. These are almost identical to the optical band gaps of bulk monoclinic ZrO_2,[15] indicating less defective lattices.[16] The tetrago-

10.1021/ja910712r

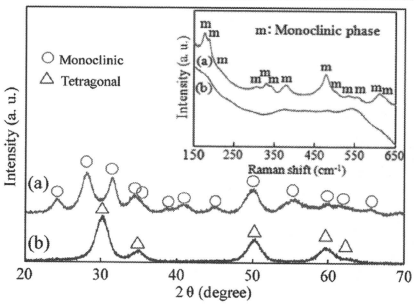

Figure 2. XRD profiles of ZrO_2 nanocrystals grown in the (a) TMAHC/TMAH and the (b) $KHCO_3$/KOH systems. The inset shows Raman spectra of colloidal solutions of ZrO_2 nanocrystals grown in the (a) TMAHC/TMAH and the (b) $KHCO_3$/KOH systems.

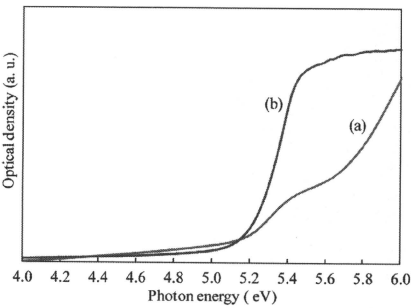

Figure 3. Optical absorption spectra of colloidal solutions of ZrO_2 nanocrystals grown in the (a) TMAHC/TMAH and the (b) $KHCO_3$/KOH systems.

nal ZrO_2 showed only one absorption shoulder at a lower photon energy (approximately at 5.1 eV) than those of monoclinic ZrO_2, indicating the presence of many lattice defects, probably cation impurity and/or oxygen vacancy.[14] Inductively coupled plasma-atomic emission spectroscopy revealed that the concentration of K^+ in the tetragonal ZrO_2 was negligible ($<10^{-7}$ mol·g^{-1}). Thus, it can be concluded that the major lattice defects in the tetragonal ZrO_2 are oxygen vacancies, which is consistent with a previous report.[16]

Here we discuss how the selective growth of monoclinic and tetragonal ZrO_2 nanocrystals was achieved. Monoclinic ZrO_2 nanocrystals may be formed due to the reduction of surface energy through capping with TMA^+, since the capping with organic substances has the potential to reduce the surface energy of oxides by more than 1.7 J·m^{-2} compared with bare surface as suggested by the literature,[10,17,18] while the surface energy of monoclinic ZrO_2 is only approximately 0.4 J·m^{-2} higher than that of tetragonal.[9] The differential thermal analysis (DTA, Figure S-2 in Supporting Information) showed that TMA^+ persists on the nanocrystals up to 280 °C. The considerably higher temperature than the vaporization temperature of free TMAH (157 °C) indicates that TMA^+ successfully caps the surface of ZrO_2 nanocrystals. By contrast, the absence of K^+ in the ZrO_2 grown in the $KHCO_3$/KOH system as shown above indicates that the K^+ does not cap the nanocrystals; thereby, the tetragonal phase is spontaneously formed.[9]

It is suggested that the energy state of surface oxygen plays a vital role in the size-dependent phase stability of ZrO_2 nanocrystals, since the stable phase strongly depends on the sign of charge of the capping agent, i.e., monoclinic ZrO_2 is obtained when the negatively charged surface oxygen is capped with oppositely charged TMA^+. By contrast, the tetragonal phase is stabilized when the nanocrystals are capped with anionic substances,[11,12] in which the surface oxygen may be exposed to the surrounding medium the same as in the case of uncapped nanocrystals ($KHCO_3$/KOH system in this study). The oxygen vacancies in the tetragonal ZrO_2 may be formed as a consequence of relaxation of the unstable surface oxygen.

In summary, our study offers a simple approach for the selective growth of pure monoclinic and tetragonal ZrO_2 nanocrystals of <10 nm diameter capped with and without TMA^+, respectively. The present concept, surface energy control via the capping with an adequate agent, is a promising universal approach to control the crystal phase of technologically important oxide nanocrystals such as Al_2O_3, TiO_2, $BaTiO_3$, and $PbTiO_3$, consequently enabling us to tune their unique properties.

Acknowledgment. This work was supported by a Scientific Research Grant from the Ministry of Education, Science, Sports and Culture of Japan.

Supporting Information Available: Size distributions of colloidal ZrO_2 nanocrystals determined by DLS method (Figure S-1); DTA analysis data of TMA^+-capped ZrO_2 nanocrystals and TMAH pentahydrate (Figure S-2). This material is available free of charge via the Internet at http://pubs.acs.org.

References

(1) Garcia-Barriocanal, J.; Rivera-Calzada, A.; Varela, M.; Sefrioui, Z.; Iborra, E.; Leon, E.; Pennycook, J.; Santamaria, J. *Science* **2008**, *321*, 676.
(2) Hoshina, T.; Wada, S.; Kuroiwa, Y.; Tsurumi, T. *Appl. Phys. Lett.* **2008**, *93*, 192914.
(3) He, D.; Ding, Y.; Luo, H.; Li, C. *J. Mol. Catal.* **2004**, *208*, 267.
(4) Wilk, G. D.; Wallace, R. M.; Anthony, J. M. *J. Appl. Phys.* **2001**, *89*, 5243.
(5) Wang G.; Meng F.; Ding C.; Chu P. K.; Liu X. *Acta Biomater.*; available online at Elsevier Sciencehttp://www.elsevier.com.
(6) Shin, J. H.; Chao, C.-C.; Huang, H.; Prinz, F. B. *Chem. Mater.* **2007**, *19*, 3850.
(7) León, C.; Lucia, M. L.; Santamaría, J. *Phys. Rev. B* **1997**, *55*, 882.
(8) Garvie, R. C.; Hannink, R. H.; Pascoe, R. T. *Nature* **1975**, *258*, 703.
(9) Garvie, R. C. *J. Phys. Chem.* **1978**, *82*, 218.
(10) Zhang, J.; Ohara, S.; Umetsu, M.; Naka, T.; Hatakeyama, Y.; Adschiri, T. *Adv. Mater.* **2007**, *19*, 203.
(11) Joo, J.; Yu, T.; Kim, Y. W.; Park, H. M.; Wu, F.; Zhang, J. Z.; Hyeon, T. *J. Am. Chem. Soc.* **2003**, *125*, 6553.
(12) Zhao, N.; Pan, D.; Nie, W.; Ji, X. *J. Am. Chem. Soc.* **2006**, *128*, 10118.
(13) Bootz, A.; Vogel, V.; Schubert, D.; Kreuter, J. *Eur. J. Pharm. Biopharm.* **2004**, *57*, 369.
(14) Michel, D.; Perez, M.; Jorba, Y.; Collongues, R. *J. Raman Spectrosc.* **1976**, *5*, 163.
(15) Kwok, C.- K.; Aita, C. R. *J. Appl. Phys.* **1989**, *66*, 2756.
(16) Yashima, M.; Tsunekawa, S. *Acta Crystallogr.* **2006**, *B62*, 161.
(17) Kaneko, K.; Inoke, K.; Freitag, B.; Hungria, A. B.; Midgley, P. A.; Hansen, T. W.; Zhang, J.; Ohara, S.; Adschiri, T. *Nano Lett.* **2007**, *7*, 421.
(18) Conesa, J. C. *Surf. Sci.* **1995**, *339*, 337.

JA910712R

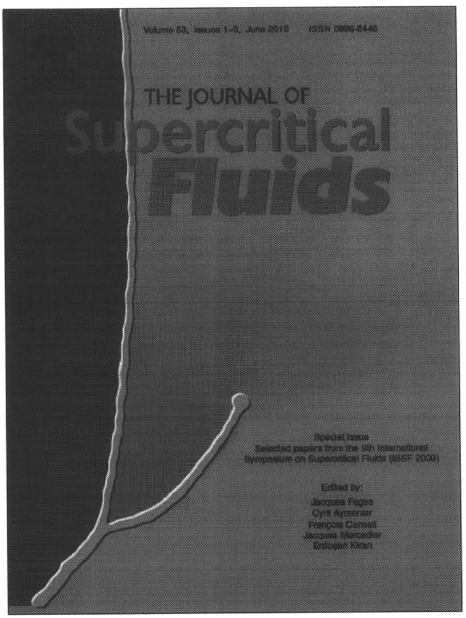

J. of Supercritical Fluids 53 (2010) 92–94

Contents lists available at ScienceDirect

The Journal of Supercritical Fluids

journal homepage: www.elsevier.com/locate/supflu

Continuous synthesis of fine $MgFe_2O_4$ nanoparticles by supercritical hydrothermal reaction

Takafumi Sasaki[a], Satoshi Ohara[a], Takashi Naka[a], Jana Vejpravova[b], Vladimir Sechovsky[b], Mitsuo Umetsu[a], Seiichi Takami[a], Balachandran Jeyadevan[c], Tadafumi Adschiri[a,*]

[a] Institute of Multidisciplinary Research for Advanced Materials, Tohoku University, 2-1-1, Katahira, Aoba-ku, Sendai 980-8577, Japan
[b] Charles University, Faculty of Mathematics and Physics, Department of Electronic Structures, Ke Karlovu 5, 121 16, Prague 2, Czech Republic
[c] Graduate School of Environmental Studies, Tohoku University, 2-1-1, Katahira, Aoba-ku, Sendai 980-8579, Japan

ARTICLE INFO

Article history:
Received 10 August 2009
Received in revised form 29 October 2009
Accepted 9 November 2009

Keywords:
Flow method
Hydrothermal synthesis
Supercritical water
$MgFe_2O_4$

ABSTRACT

We produced magnesium ferrite ($MgFe_2O_4$) nanoparticles by hydrothermal synthesis in supercritical water. Suspensions containing varying ratios of $Mg(OH)_2$ and $Fe(OH)_3$ at room temperature were pressurized to 30 MPa, fed into a tubular reactor by high-pressure pump, and rapidly heated to reaction temperature by mixing with supercritical water. The $MgFe_2O_4$ phase forms at 460 °C. The Mg/Fe molar ratio was varied from 0.5 to 1.5 with the goal of obtaining single-phase $MgFe_2O_4$. At the stoichiometric ratio for $MgFe_2O_4$, Mg/Fe = 0.5, the product contains both $MgFe_2O_4$ and α-Fe_2O_3. At Mg/Fe = 1.0 and 1.5, the product is the desired single-phase $MgFe_2O_4$. The synthesized $MgFe_2O_4$ nanoparticles, with particle size of about 20 nm, exhibit superparamagnetic behavior.

1. Introduction

Magnetic particles, whose properties depend on their size, have been studied for applications such as catalysis, energy storage, high-density data storage, and ferrofluids [1]. Magnetic particles of nanometer-range size are useful in biotechnology applications such as magnetic separation, magnetic resonance imaging, and magnetic hyperthermia treatment [2]. Magnetic hyperthermia treatment involves the breakdown of cancer cells at 42–45 °C. Magnetic particles generate heat in the presence of a magnetic field; the degree of magnetic heating depends on particle size and magnetic properties [3]. Among candidate particles for use in magnetic hyperthermia treatment, magnetite and maghemite have been best studied to date because of their magnetic properties and biological compatibility [4,5], and $MgFe_2O_4$ particles of micrometer-range size are reported to exhibit greater magnetic heating than do other ferrites [6]. Recently, magnetic hyperthermia treatment has been investigated for use in conjunction with a drug delivery system (DDS) so as to enable heating of only cancer tissue. A requirement for use with a DDS is that particle size must be in the range 10–100 nm for accumulation in cancer tissue [7]. Therefore, synthesis of $MgFe_2O_4$ nanoparticles of precisely controlled size is of great interest.

$MgFe_2O_4$ nanoparticles can be synthesized by milling, but particles thus produced lack uniform size and morphology [8,9]. Zhang and co-workers [10] synthesized the nanoparticles by the reverse micelle method and Willey et al. [11,12] by sol–gel supercritical drying, but in both cases, the synthesis at lower temperature may results in the inclusion of impurities that are not favorable for human body. Joy and co-workers [13] synthesized the nanoparticles by microwave hydrothermal treatment, but the product lacked sufficient crystallinity.

We have developed a hydrothermal synthesis method for forming advanced metal-oxide particles in supercritical water [14], and other researchers have also prepared fine metal–oxide particles by this method [15–18]. Some important advantages of supercritical hydrothermal synthesis of particles are as follows: (i) nanoparticle formation; (ii) single-crystal formation with a high level of crystallinity; (iii) capability to control particle size and morphology to some extent with pressure and temperature; and (iv) capability to create a homogeneous reducing or oxidizing atmosphere by introduction of gases or additional compounds (O_2, H_2). We report herein the synthesis of fine $MgFe_2O_4$ nanoparticles in supercritical water using a flow-type apparatus, and the evaluation of their magnetic properties.

2. Material and methods

Iron (III) nitrate solution ($Fe(NO_3)_3{\cdot}9H_2O$, Kojundo Chemical Laboratory Co., Ltd., 99.9% purity) was prepared at fixed

Abbreviations: DDS, drug delivery system; FC, field-cooling; SQUID, superconconducting quantum interface device; TEM, transmission electron microscopy; VSM, vibrating sample magnetometer; XRD, X-ray diffraction; ZFC, zero-field-cooling.

* Corresponding author. Tel.: +81 22 217 5629; fax: +81 22 217 5629.
E-mail address: ajiri@tagen.tohoku.ac.jp (T. Adschiri).

0896-8446/$ – see front matter © 2009 Elsevier B.V. All rights reserved.
doi:10.1016/j.supflu.2009.11.005

concentrations of 0.01 or 0.005 M. Magnesium nitrate solution ($Mg(NO_3)_2{\cdot}6H_2O$, Kojundo Chemical Laboratory Co., Ltd., 99.0% purity) was also prepared at concentrations so as to vary the Mg/Fe molar ratio from 0.5 to 1.5. The metal nitrate solutions were mixed with equivalent amount of potassium hydroxide solution (KOH, Wako Pure Chemical Industries, Ltd.), and $Fe(OH)_3$ and $Mg(OH)_2$ precipitates were formed. The resulting precipitates were separated by centrifugation and washed with distilled water two times. Finally, $Fe(OH)_3$ and $Mg(OH)_2$ mixed suspensions were prepared by dilution with distilled water.

The flow-type apparatus used in this study has been described in detail elsewhere [14]. Metal oxides suspension was pressurized at 30 MPa and fed into a reactor by high-pressure pump (flow rate 1 mL/min). Distilled water was also pressurized and fed through another line by another high-pressure pump (flow rate 10 mL/min), and then heated by electric furnace to a pre-determined temperature. The suspension was mixed with the supercritical water at a junction in the reactor, which rapidly heated the mixture up to the reaction temperature. After mixing, the reactants went through a tube whose temperature was kept at the reaction temperature. The length, diameter, and volume of the tube at this isothermal zone were 50 cm, 0.18 cm, and 0.77 cm^3, respectively. Residence time at the isothermal zone of 400 and 460 °C was 2.4 and 0.9 s, respectively. At the exit of the reactor, the fluid was rapidly cooled by an external water jacket. The reaction temperature was varied from 400 to 460 °C by controlling the temperature of distilled water and the Mg/Fe molar ratio was varied from 0.5 to 1.5 with the goal of obtaining single-phase $MgFe_2O_4$. Synthesized nanoparticles were collected by in-line filtration, washed with distilled water and HNO_3 solution to remove $Mg(OH)_2$, and then dried in an oven at 60 °C.

Particle structure was determined by X-ray diffractometer (XRD; Rigaku RINT 2000 system with a Cu-Kα_1 beam). Particle morphology was observed by transmission electron microscopy (TEM; JEOL, Ltd., JEM-1200EX). Composition ratio of Mg:Fe in the products was measured by inductively coupled plasma (ICP; PerkinElmer Co., Ltd., Optima 3300) analysis. Magnetic properties were measured by vibrating sample magnetometer (VSM; Tamakawa Co., Ltd., TM-VSM1230-HHHS) and superconducting quantum interface device magnetometer (Quantum Design, MPMS).

3. Results and discussion

First, we investigated the effect of temperature on the formation of $MgFe_2O_4$. Fig. 1 shows XRD patterns of the products synthesized with Mg/Fe = 0.5 at 400 and 460 °C. At 400 °C, the product is mostly $MgFe_2O_4$ phase (designated ●); α-Fe_2O_3 (designated ■)

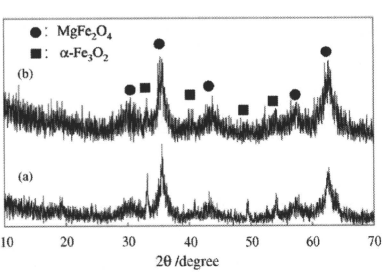

Fig. 1. XRD profiles of particles synthesized at Mg/Fe = 0.5, 30 MPa, and various temperatures: (a) 400 °C; (b) 460 °C.

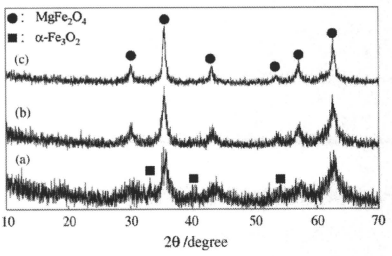

Fig. 2. XRD profiles of particles synthesized at 460 °C, 30 MPa, and various Mg/Fe molar ratios: (a) Mg/Fe = 0.5; (b) Mg/Fe = 1.0; (c) Mg/Fe = 1.5.

phase also forms but as an impurity. At 460 °C, the amount of α-Fe_2O_3 product decreases. In general, metal oxide is formed through dissolution and recrystallization processes of hydroxide precursors in aqueous solution. In this study, $MgFe_2O_4$ was formed through dissolution–recrystallization of $Fe(OH)_3$ and $Mg(OH)_2$ at elevated temperature. In order to confirm the solubility of $Mg(OH)_2$ at elevated temperature, we have investigated the effect of temperature on the formation of MgO using batch type reactor. A $Mg(OH)_2$ suspension was loaded into a batch reactor and heated by electric furnace. The reaction temperature was changed from 400 to 600 °C and the pressure was fixed to 30 MPa. XRD measurements showed that MgO phase was formed only at 600 °C. The result means that the solubility of $Mg(OH)_2$ becomes higher with increasing temperature. It indicates that dissolution of $Mg(OH)_2$ at higher temperature leads to form $MgFe_2O_4$. Furthermore, formation of α-Fe_2O_3 is inhibited due to rapid increase in temperature. Even at the higher temperature, single-phase $MgFe_2O_4$ product does not form at Mg/Fe = 0.5, possibly because the $Fe(OH)_3$ precursor is unable to react with $Mg(OH)_2$ and forms α-Fe_2O_3 as an impurity.

Second, we investigated the effect of the Mg/Fe molar ratio to improve the phase purity. Fig. 2 shows XRD patterns of the products for Mg/Fe = 0.5, 1.0, and 1.5. For Mg/Fe = 0.5, the product contains α-Fe_2O_3 (designated ■). For Mg/Fe = 1.0 and 1.5, $MgFe_2O_4$ (designated ●) forms in a single phase. Furthermore, ICP measurement of the particles synthesized with Mg/Fe = 1.0 was conducted. The result shows that the composition ratio of Mg:Fe is 1.0:2.3. The conversion ratio from $Mg(OH)_2$ to MgO reaches the ratio for forming only $MgFe_2O_4$. Such a nonstoichiometric synthesis of barium hexaferrite using a flow-type apparatus was also reported by Hakuta et al. [19]. Fig. 3 shows a TEM image of the synthesized $MgFe_2O_4$ nanoparticles. The average size of the particles is calculated as 16.5 nm with a standard deviation of 3 nm (17.8%) by counting 100 particles taken from TEM images. Generally speaking, separation of nucleation and growth periods is a key to forming monodispersed particles. In a flow-type apparatus, a large degree of supersaturation is obtained easily and renucleation is inhibited during reaction because the reaction solution is heated rapidly; therefore, the particle size is smaller than for particles synthesized by batch reactor [20].

Finally, we investigated magnetization of the synthesized $MgFe_2O_4$ nanoparticles. After a sample is cooled from room temperature to 2.0 K under a magnetic field (field-cooling, FC) at 200 Oe, susceptibility decreases monotonically with increasing temperature (Fig. 4a). In contrast, after a sample is cooled similarly but without external magnetic field (zero-field-cooling, ZFC), magnetization increases and reaches a maximum at the so-called blocking temperature; in this case, T = 94 K (Fig. 4b). Magnetization after ZFC coincides with that after FC above $T \sim 100$ K. These irreversible behaviors are characteristic of superparamagnetism [21]. Magne-

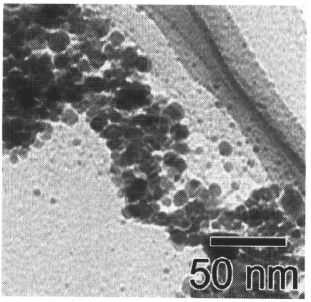

Fig. 3. TEM image of $MgFe_2O_4$ nanoparticles synthesized at 460 °C, 30 MPa, Mg/Fe = 1.0.

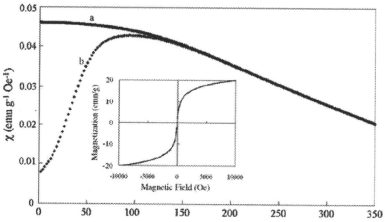

Fig. 4. Plot of magnetic susceptibility vs temperature and magnetization curve (inset) for $MgFe_2O_4$ nanoparticles synthesized at 500 °C, 30 MPa, Mg/Fe = 1.0.

tocrystalline anisotropy E_A decreases with decreasing particle size because E_A is proportional to KV, where K is the magnetocrystalline anisotropy constant and V is the nanoparticle size. For thermal activation energy k_BT, where k_B is the Boltzmann constant, at $E_A < k_BT$, the magnetic moment of the particle fluctuates randomly, showing paramagnetic character; at $E_A > k_BT$, the magnetic moment of an individual ferromagnetic particle aligns along the axis of easy magnetization. For ZFC, magnetic moments are randomly oriented, and consequently the total magnetic moment of the powder sample becomes zero; for FC, field-induced moments are quenched. The magnetization curve at 298 K indicates that the coercivity force is less than 10 Oe (Fig. 4 inset).

4. Conclusions

We succeeded in synthesizing single-phase $MgFe_2O_4$ nanoparticles by supercritical hydrothermal synthesis in a flow-type apparatus. At 460 °C, 30 MPa, and Mg/Fe = 1.0 and 1.5, we obtained single-phase $MgFe_2O_4$ nanoparticles. For successful synthesis of the single phase, high reaction temperature and nonstoichiometric conditions are important. The obtained nanoparticles are about 20 nm in size and exhibit superparamagnetic behavior.

References

[1] Q.A. Pankhurst, R.J. Pollard, Fine-particle magnetic oxides, J. Phys.: Condens. Matter 5 (1993) 8487–8508.
[2] Q.A. Pankhurst, J. Connoly, S.K. Jones, J. Dobson, Applications of magnetic nanoparticles in biomedicine, J. Phys. D: Appl. Phys. 36 (2003) R167–R181.
[3] S. Mornet, S. Vasseur, F. Grasset, E. Duguet, Magnetic nanoparticle design for medical diagnosis and therapy, J. Mater. Chem. 14 (2004) 2161–2175.
[4] L.E. Bioa, M. Shinkai, T. Kitade, H. Honda, J. Yoshida, T. Wakabayashi, T. Kobayashi, Preparation of tumor-specific magnetoliposomes and their application for hyperthermia, J. Chem. Eng. Jpn. 34 (2001) 66–72.
[5] Y. Jun, J.-H. Lee, J. Cheon, Chemical design of nanoparticle probes for high-performance magnetic resonance imaging, Angew. Chem. Int. Ed. 47 (2008) 5122–5135.
[6] T. Maehara, K. Konishi, T. Kamimori, H. Aono, H. Hirazawa, T. Naohara, S. Nomura, H. Kikkawa, Y. Watanabe, K. Kawachi, Selection of ferrite powder for thermal coagulation therapy with alternating magnetic field, J. Mater. Sci. 40 (2005) 135–138.
[7] T. Watanabe, H. Ichikawa, Y. Fukumori, Tumor accumulation of gadolinium in lipid-nanoparticles intravenously injected for neutron-capture therapy of cancer, Eur. J. Pharm. Biopharm. 54 (2002) 119–124.
[8] V. Šepelák, D. Schultze, F. Krumeich, U. Steinike, K.D. Becker, Mechanically induced cation redistribution in magnesium ferrite and its thermal stability, Solid State Ionics 141–142 (2001) 677–682.
[9] V. Šepelák, M. Menzel, K.D. Becker, F. Krumeich, Mechanochemical reduction of magnesium ferrite, J. Phys. Chem. B 106 (2002) 6672–6678.
[10] C. Liu, B. Zou, A.J. Rondinone, Z.J. Zhang, Chemical control of superparamagnetic properties of magnesium and cobalt spinel ferrite nanoparticles through atomic level magnetic couplings, J. Am. Chem. Soc. 122 (2000) 6263–6267.
[11] R.J. Willey, S.A. Oliver, G. Oliveri, G. Busca, Chemistry and structure of mixed magnesium ferric-oxide aerogels, J. Mater. Res. 8 (1993) 1418–1427.
[12] R.J. Willey, P. Noirclerc, G. Busca, Preparation and characterization of magnesium chromite and magnesium ferrite aerogels, Chem. Eng. Commun. 123 (1993) 1–16.
[13] S. Verma, P.A. Joy, Y.B. Khollam, H.S. Potdar, S.B. Deshpande, Synthesis of nanosized $MgFe_2O_4$ powders by microwave hydrothermal method, Mater. Lett. 58 (2004) 1092–1095.
[14] T. Adschiri, Y. Hakuta, K. Sue, K. Arai, Hydrothermal synthesis of metal oxide nanoparticles at supercritical conditions, J. Nanoparticle Res. 3 (2001) 227–235.
[15] A. Cabañas, J.A. Darr, E. Lester, M. Poliakoff, Continuous hydrothermal synthesis of inorganic materials in a near-critical water flow reactor; the one-step synthesis of nano-particulate $Ce_1-xZr_xO_2$ ($x = 0-1$) solid solutions, J. Mater. Chem. 11 (2001) 561–568.
[16] R. Viswanathan, R.B. Gupta, Formation of zinc oxide nanoparticles in supercritical water, J. Supercrit. Fluids 27 (2003) 187–193.
[17] F. Cansell, C. Aymonier, Design of functional nanostructured materials using supercritical fluids, J. Supercrit. Fluids 47 (2009) 508–516.
[18] C. Aymonier, A. Loppinet-Serani, H. Reverón, Y. Garrabos, F. Cansell, Review of supercritical fluids in inorganic materials science, J. Supercrit. Fluids 38 (2006) 242–251.
[19] Y. Hakuta, T. Adschiri, T. Suzuki, T. Chida, K. Seino, K. Arai, Flow method for rapidly producing barium hexaferrite particles in supercritical water, J. Am. Ceram. Soc. 81 (1998) 2461–2464.
[20] K. Sue, K. Murata, K. Kimura, K. Arai, Continuous synthesis of zinc oxide nanoparticles in supercritical water, Green Chem. 5 (2003) 659–662.
[21] Q. Chen, Z.J. Zhang, Size-dependent superparamagnetic properties of $MgFe_2O_4$ spinel ferrite nanocrystallites, Appl. Phys. Lett. 73 (1998) 3156–3158.

Arrangement of palladium nanoparticles templated by supramolecular self-assembly of SDS wrapped on single-walled carbon nanotubes†

Zhenquan Tan,* Hiroya Abe, Makio Naito and Satoshi Ohara

Received 24th February 2010, Accepted 21st April 2010
First published as an Advance Article on the web 13th May 2010
DOI: 10.1039/c0cc00099j

We report a facile route to selectively deposit and arrange palladium (Pd) nanoparticles on single-walled carbon nanotubes (SWCNTs) having sub 10 nm diameter by using supramolecular self-assembly of sodium dodecyl sulfate (SDS) as a soft template.

Carbon nanotubes (CNTs) have been one of the most extensively studied nanostructured materials over the last decade because of their potential applications in many fields.[1] In particular, surface functionalization and hybridization of CNTs currently attracts significant research interest because CNTs are ideal templates for the decoration of functional nanoparticles.[2] Such decoration of CNTs leads to the design and construction of various heterogeneous nanocomposites with functionalities including high-performance catalytic activity, fuel cell capabilities and (bio)chemical sensors.

One of the most attractive topics in the functionalization and hybridization of CNTs is to construct controllable heterogeneous nanostructures on CNTs with sub ten nanometers diameter. Polymers seem to be a sweet candidate towards this objective. Li's group reported the formation of alternating periodic patterns of copolymers on CNTs.[3] Based on this approach, they succeeded in the immobilization of gold nanoparticles on the block copolymer/CNT hybrid to construct designed heterogeneous nanostructures on CNTs.[3d] Actually, many organic molecules are reported to form ordered nanostructures on CNTs.[4] Some of them are suitable to arrange metal nanoparticles or quantum dots on CNTs.

Surfactant-functionalized CNTs are now also considered as another charming approach to control the heterogeneous nanostructures on CNTs. Surfactants have been widely studied because of the advantages of dispersing CNTs in water and changing the surface physical properties of CNTs.[5] SDS is a generally used surfactant to disperse and functionalize CNTs in water.[6] Richard *et al.* discovered that SDS forms a supramolecular self-assembly with a half-cylinder structure on the surface of CNTs.[7] The nanostructural pattern of SDS-functionalized CNTs represents an ideal template to construct designed heterogeneous nanostructures on CNTs. In this study, we report the site-selective deposition and patterning of Pd nanoparticles on SWCNTs by utilizing the supramolecular self-assembly of SDS acting as a soft template. There are four advantages with using SDS as a soft temple. At first, SDS is highly effective at dissolving SWCNTs in water, which is very important for solution chemistry of SWCNTs. Secondly, SDS can form supramolecular self-assembly on SWCNTs, which is an ideal soft template to arrange nanoparticles or quantum dots on SWCNTs. Thirdly, SDS is a small molecule and is hydrophobically bonding with SWCNTs. This makes it easy to remove SDS from SWCNTs by alcohol washing and filtration. Finally, SDS is an environment-friendly reagent, and is very easy to obtain. It would not cause additional cost request. On the other hand, since Pd nanoparticles have great applications in fuel cell, high-performance catalyst and hydrogen storage,[8] it is of many scientific interests to construct one-dimensional Pd nanostructures on SWCNTs.

The experimental approach for the arrangement of Pd nanoparticles on SDS-functionalized SWCNTs is described in Scheme 1. At first, the big bundles of SWCNTs are separated into individual and/or small bundle tubes by forming supramolecular self-assembly of SDS half-cylinders on the surface of SWCNTs.[9] Secondly, Pd(II) ions are selectively absorbed on the surface of SDS supramolecular self-assembly due to the electrostatic interaction between Pd(II) cation and the anionic groups of sulfate in SDS molecules. Finally, Pd nanoparticles with sub five nanometers size are synthesized on the nanotubes by a photoreduction reaction and form helical nanostructures wrapped around the SWCNTs templated by SDS supramolecular self-assembly.

We characterized the pristine SWCNTs by scanning electron microscopy (SEM, Hitachi, Japan). The pristine SWCNTs are almost large bundles having an average diameter of 50 nm (Fig. 1A). The bundles twisted together due to the van der Waals interaction. After dispersing in SDS aqueous solution, the large bundles of pristine SWCNTs were effectively separated into small bundles and/or individual SWCNTs, as observed by transmission electron microscopy (TEM, JEM-2100F, JEOL) (Fig. 1B). Actually, SDS molecules were formed by ordered supramolecular self-assembly

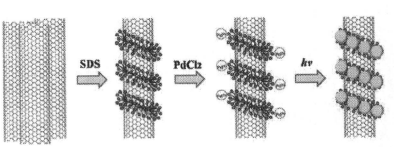

Scheme 1 A schematic approach for the site-selective synthesis of ordered nanostructures of Pd nanoparticles wrapped on SWCNTs.

Joining and Welding Research Institute, Osaka University, 11-1 Mihogaoka, Ibaraki, Osaka 567-0047, Japan. E-mail: zq-tan@jwri.osaka-u.ac.jp; Fax: +816 6879 4370; Tel: +816 6879 4370

† Electronic supplementary information (ESI) available: Experimental details. See DOI: 10.1039/c0cc00099j

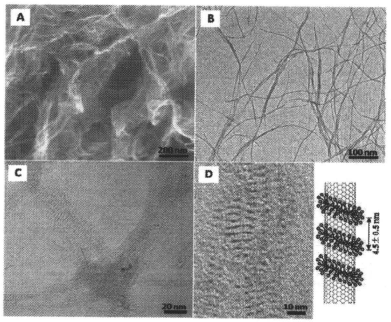

Fig. 1 (A) SEM image of pristine SWCNTs, and (B) TEM image of SDS functionalized SWCNTs. (C) and (D) High-resolution TEM images of SDS functionalized SWCNTs.

on the surface of CNTs.[7] Fig. 1C shows a high-resolution TEM photograph of SDS-functionalized SWCNTs. We can clearly observe the supramolecular self-assembly of SDS half-cylinders wrapped on the surface of SWCNTs. Furthermore, the ordered nanostructures of SDS with varying tilt angles can be clearly observed in a magnification photograph shown in Fig. 1D. The tilt angles of helices depend on the diameter of the CNTs.[7] The lateral striations of SDS supramolecular self-assembly were 4.5 ± 0.5 nm. This value is in good agreement to the previous research.[7] The supramolecular self-assembly of SDS half-cylinders provide a sweet soft template to arrange metal nanoparticles on SWCNTs to form ordered heterogeneous nanostructures.

The photoreduction reaction of palladium chloride in the suspension of SDS-functionalized SWCNTs was characterized by the UV-Vis absorption spectroscopy (see Supporting Information Fig. S1†). The palladium chloride aqueous solution shows a clear absorption at 420 nm, which originates from the *d–d* electron transition of Pd(II) ions.[10] The SDS-functionalized SWCNTs aqueous solution shows numerous absorption peaks between 400 and 800 nm which originate from the van Hove maxima electronic density of the quasi one-dimensionality of the SWCNTs.[11] The absorption band of Pd(II) ions at 420 nm disappeared completely when Pd nanoparticles were reduced and deposited on SWCNTs.

The resulting nanostructures of Pd nanoparticles on the surface of SDS-functionalized SWCNTs were characterized by high-resolution TEM. It is clearly observed that Pd nanoparticles formed ordered nanostructures that the Pd nanoparticles arranged on the surface of SWCNTs (Fig. 2A). These nanostructures are very similar to those using copolymers as a soft template.[4] Since SDS, the soft template, formed periodic supramolecular self-assembly on SWCNTs, the deposited Pd nanoparticles also formed ordered periodic nanostructures on the surface of SWCNTs. Such periodic nanostructures were clearly observed by high-resolution TEM (Fig. 2B). The Pd nanoparticles have a size of 2.5 ± 0.5 nm. The inter-nanoparticle distance was 4.5 ± 0.5 nm along the orientation parallel to the tube axis. This value is the same as the lateral striations of SDS half-cylinders that are shown in Fig. 1C. This observation indicates that the Pd nanoparticles were selectively deposited onto the SDS-functionalized SWCNTs along the half-cylinders of SDS supramolecular self-assemblies wrapped around the SWCNTs. The ordered nanostructures of Pd nanoparticles were observed in detail (Fig. 2C–E). Fig. 3C shows a clear image of Pd nanoparticles forming ordered nanostructures wrapped around the SWCNTs. The nanostructures have a right helix twist with a tilt angle of $-6°$ relative to the tube axis. The tilt angle of Pd nanostructures depends on the SDS half-cylinders acting as a soft template. In our experiment, the ordered nanostructures of Pd nanoparticles with various helices or tilt angles were also observed (Fig. 2D). Interestingly, periodic nanostructures of Pd nanoparticles with various helices and tilt angles were also observed on an individual bundle of SWCNTs (Fig. 2E). It indicates that the various helices of half-cylinders of SDS supramolecular self-assembly were wrapped around an individual SWCNTs. Fig. 3F shows a high resolution TEM image of the Pd nanoparticle signalled by the arrow in Fig. 2E. The ordered lattice of Pd atoms can be clearly observed. The crystallinity of Pd nanoparticles were also confirmed by powder X-ray diffraction (XRD) measurement (see Supporting Information Fig. S2†). Fig. 2G shows a dark field STEM image of Pd nanoparticles wrapped around SWCNTs. The ordered

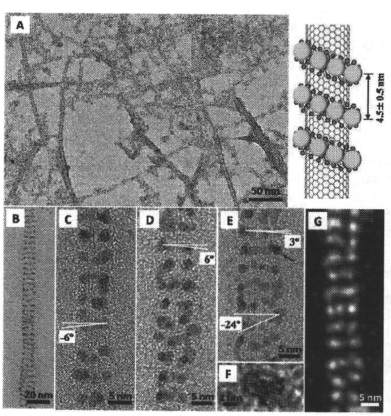

Fig. 2 TEM images of (A) Pd nanoparticles selectively deposited on the SDS-functionalized SWCNTs, (B) Pd nanoparticles form a unique helical nanostructure wrapped around a nanotube. (C) Pd nanoparticles wrapped in a right helix with a tilt angle of $-6°$ relative to the nanotube axis. (D) Pd nanoparticles wrapped in a left helix around a SWCNT with a tilt angle of 6° relative to the tube axis. (E) Pd nanoparticles organized as a left helix wrapped around the tube with a tilt angle of 3° and a right helix with a tilt angle of $-24°$ relative to the nanotube axis. (F) A high resolution TEM image of Pd nanoparticle. (G) A dark field STEM image of Pd nanoparticles wrapped around a small bundle of SWCNTs.

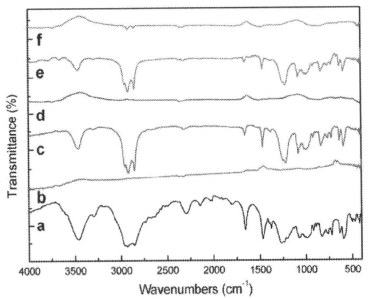

Fig. 3 ATR infrared spectrum of (a) SDS, (b) pristine SWCNTs, (c) SDS-functionalized SWCNTs, (d) SDS-functionalized SWCNTs after alcohol washing, (e) Pd nanoparticles decorated SWCNTs, and (f) Pd nanoparticles decorated SWCNTs after washing.

nanostructures of Pd nanoparticles arranged on SWCNTs were also clearly confirmed by the STEM observation.

The interaction between SDS molecules and SWCNTs were characterized by attenuated total reflectance (ATR) infrared spectrometry (IRPrestige-21, Shimadzu) in KBr matrix (Fig. 3). The pristine SDS showed absorption peaks at 2957, 2928 and 2853 cm^{-1} (C–H stretching), 1468 and 1377 cm^{-1} (C–H bending), 1267, 1236 and 1206 cm^{-1} ($-OSO_3^-$ stretching).[12] A prominent absorption band at 3460 cm^{-1} in SDS spectrum was due to the O–H stretching vibration of absorbed water. SWCNTs have no obvious IR absorption band from 4000 to 1000 cm^{-1} in our measurement (Fig. 3B). When SDS was adsorbed on SWCNTs, Fig. 3C shows the IR absorption peaks of SDS were slightly shifted to lower frequency region (C–H stretching at 2955, 2918, 2845 cm^{-1}, C–H bending at 1467 and 1376 cm^{-1}, $-OSO_3^-$ stretching at 1246, 1217, 1082 cm^{-1}). These shifts may be attributed to the formation of hydrophobic bonds between SDS and SWCNTs. The IR absorption peaks of SDS-functionalized SWCNTs disappeared from view after alcohol washing and filtration (Fig. 3D). The ATR infrared spectrum was very similar to that of pristine SWCNTs. It proves that SDS molecules were removed from the surface of SWCNTs by alcohol washing. Even decorated by Pd nanoparticles, the ATR infrared spectrum of SDS was almost the same with that absorbed on SWCNTs (Fig. 3E). When Pd nanoparticles-decorated SWCNTs were washed and filtrated, the absorption peaks of SDS were dramatically decreased and its intensity is just approximate to that of the CO_2 absorption peak at 2355 cm^{-1} (Fig. 3F). It indicates that SDS was almost removed from SWCNTs. This result suggests that SDS can be removed effectively from SWCNTs if they would degrade performance of the ordered nanostructures.

In summary, a facile route is reported to site-selectively deposit and arrange metal nanoparticles on the surface of SWCNTs having sub 10 nm diameter. SDS formed supramolecular self-assembly of half-cylinders wrapped around SWCNTs, and acted as a soft template to selectively deposit metal nanoparticles. Pd nanoparticles have been arranged on the surface of SWCNTs and formed ordered periodic nanostructures templated by SDS supramolecular self-assembly. Actually, this facile approach is easily applied to arrange a variety of metal nanoparticles and/or quantum dots on SWCNTs. Since many organic molecules, such as surfactant, polymer and DNA, form supramolecular nanostructures wrapped around CNTs, this facile approach represents a potential and simple chemical route to arrange nanoparticles and/or quantum dots to form ordered heterogeneous nanostructures on CNTs by utilizing such surfactant, polymers or DNA as a soft template.

This work was partially supported by a Scientific Research Grant from the Ministry of Education, Culture, Sports, Science and Technology of Japan.

Notes and references

1 (*a*) L. Qu, L. Dai and E. Osawa, *J. Am. Chem. Soc.*, 2006, **128**, 5523; (*b*) M. A. Correa-Duarte, J. Pérez-Juste, A. Sánchez-Iglesias, M. Giersig and L. M. Liz-Marzán, *Angew. Chem., Int. Ed.*, 2005, **44**, 4375; (*c*) G. G. Wildgoose, C. E. Banks and R. G. Compton, *Small*, 2006, **2**, 182.

2 P. M. Ajayan and J. M. Tour, *Nature*, 2007, **447**, 1066.

3 (*a*) C. Y. Li, L. Y. Li, W. W. Cai, S. L. Kodjie and K. K. Tenneti, *Adv. Mater.*, 2005, **17**, 1198; (*b*) L. Li, Y. Yang, G. Yang, X. Chen, B. S. Hsiao, B. Chu, J. E. Spanier and C. Y. Li, *Nano Lett.*, 2006, **6**, 1007; (*c*) L. Li, C. Y. Li and C. Ni, *J. Am. Chem. Soc.*, 2006, **128**, 1692; (*d*) B. Li, L. Li, B. Wang and C. Y. Li, *Nat. Nanotechnol.*, 2009, **4**, 358.

4 (*a*) M. Zheng, A. Jagota, E. D. Semke, B. A. Diner, R. S. McLean, S. R. Lustig, R. E. Richardson and N. G. Tassi, *Nat. Mater.*, 2003, **2**, 338; (*b*) A. Nish, J.-Y. Hwang, J. Doig and R. J. Nicholas, *Nat. Nanotechnol.*, 2007, **2**, 640; (*c*) C. Thauvin, S. Rickling, P. Schultz, H. Celia, S. Meunier and C. Mioskowski, *Nat. Nanotechnol.*, 2008, **3**, 743; (*d*) S.-Y. Ju, J. Doll, I. Sharma and F. Papadimitrakopoulos, *Nat. Nanotechnol.*, 2008, **3**, 356; (*e*) S.-Y. Ju, W. P. Kopcha and F. Papadimitrakopoulos, *Science*, 2009, **323**, 1319; (*f*) X. Tu, S. Manohar, A. Jagota and M. Zheng, *Nature*, 2009, **460**, 250.

5 (*a*) W. Wenseleers, I. I. Vlasov, E. Goovaerts, E. D. Obraztsoca, A. S. Lobach and A. Bouwen, *Adv. Funct. Mater.*, 2004, **14**, 1105; (*b*) M. C. Hersam, *Nat. Nanotechnol.*, 2008, **3**, 387.

6 (*a*) M. Burghard, G. Duesberg, G. Philipp, J. Muster and S. Roth, *Adv. Mater.*, 1998, **10**, 584; (*b*) M. J. O'Connell, S. M. Bachilo, C. B. Huffman, V. C. Moore, M. S. Strano, E. H. Haroz, K. L. Rialon, P. J. Boul, W. H. Noon, C. Kittrell, J. Ma, R. H. Hauge, R. B. Weisman and R. E. Smalley, *Science*, 2002, **297**, 593.

7 C. Richard, F. Balavoine, P. Schultz, T. W. Ebbesen and C. Mioskowski, *Science*, 2003, **300**, 775.

8 (*a*) Y. Hatakeyama, M. Umetsu, S. Ohara, F. Kawadai, S. Takami, T. Naka and T. Adschiri, *Adv. Mater.*, 2008, **20**, 1122; (*b*) Y.-H. Chen, H.-H. Hung and M. H. Huang, *J. Am. Chem. Soc.*, 2009, **131**, 9114; (*c*) D. G. Narehood, S. Kishore, H. Goto, J. H. Adair, J. A. Nelson, H. R. Gutirrez and P. C. Eklund, *Int. J. Hydrogen Energy*, 2009, **34**, 952.

9 (*a*) H. Xu, H. Abe, M. Naito, H. Ichikawa, Y. Fukumori and S. Endoh, *J. Ceram. Soc. Jpn.*, 2008, **116**, 965; (*b*) Z. Tan, H. Xu, H. Abe, M. Naito and S. Ohara, *J. Nanosci. Nanotechnol.*, 2010, **10**, 3978.

10 L. I. Elding and L. F. Olsson, *J. Phys. Chem.*, 1978, **82**, 69.

11 S. M. Bachilo, M. S. Strano, C. Kittrell, R. H. Hauge, R. E. Smalley and R. B. Weisman, *Science*, 2002, **298**, 2361.

12 (*a*) K. D. Dobson, A. D. Roddick-Lanzilotta and A. J. McQuillan, *Vib. Spectrosc.*, 2000, **24**, 287; (*b*) R. P. Sperline, *Langmuir*, 1997, **13**, 3715.